Article

Sequential layer-by-layer deposition for high-performance fully thermal-evaporated red perovskite light-emitting diodes

Yajing Li[1], Na Meng[1], Yutian Xu[1], Bufan Yu[2], Junhao Liu[1], Yuanhao Cui[1], Ziqiang Wang[1], Xinwu Ke[1], Tengfei Pan[1], Xue Min[1], Jiangshan Chen [2], Dongge Ma [2], Lingfeng Chao[1], Zhelu Hu[1], Yingdong Xia[1] ✉, Qingxun Guo [1] ✉, Yonghua Chen [1] ✉ & Wei Huang [1,3] ✉

Thermal-evaporated perovskite light-emitting diodes are highly promising for future display and lighting. However, multi-source co-evaporation faces challenges such as difficulty in regulating crystallinity, especially for red perovskite light-emitting diodes, whose external quantum efficiencies are still less than 2%. Here, we demonstrate a facile layer-by-layer thermal-evaporation strategy to fabricate high-quality perovskite-emitting films with tunable emission wavelengths. 5-Aminovaleric acid is introduced to regulate interfacial reactions during deposition, slow down crystallization during post-annealing, and passivate defects through coordination interactions. This approach yields perovskite emitting layers with high uniformity and luminance efficiency. As a result, red (670 nm) and deep-red (730 nm) perovskite light-emitting diodes achieve maximum external quantum efficiencies of 9% and 7.27%, and luminance of over 1500 cd m⁻² and 200 W s⁻¹ m⁻², respectively. Furthermore, large-area (2500 mm²) and patterned perovskite thin films and light-emitting diodes with outstanding uniformity are successfully demonstrated.

In recent years, metal halide perovskite materials possess excellent optoelectronic properties, including tunable band gap, high defect tolerance, high quantum yield, etc, making them highly suitable for the fabrication of high-performance light-emitting diodes (LEDs)[1–6]. Since the first demonstration of room-temperature electroluminescence from perovskite light-emitting diodes (PeLEDs) in 2014, the external quantum efficiency (EQE) of red and green PeLEDs has soared from less than 0.1% to over 30% within just a few years[7–11]. However, high-efficiency PeLEDs rely primarily on solution-based fabrication methods, which face challenges in large-area uniformity and reproducibility[12]. In contrast, PeLEDs fabricated through thermal evaporation hold the potential for large-scale manufacturing, leveraging existing production lines, e.g., organic LEDs (OLEDs) display industry technologies. Notably, thermal-evaporated green and blue PeLEDs have achieved an EQE of 16.4% and 10.41%[13,14], respectively, demonstrating the immense potential of vacuum deposition techniques. However, research on red-emitting PeLEDs fabricated via thermal evaporation remains limited. One of the earliest reports employed CsSnBr₃ as the emissive layer, achieved through the evaporation of CsBr and SnBr₂, followed by annealing[15]. Subsequently, Zeng et al. realized red emission from CsPbI₂Br films by co-evaporating CsBr and PbI₂, with crystallization optimized through heating-assisted vacuum deposition[16]. To reduce defect density and enhance emission efficiency, Liu et al. introduced a dual-interface modification strategy

¹State Key Laboratory of Flexible Electronics (LoFE) & Institute of Advanced Materials (IAM), School of Flexible Electronics (Future Technologies), Nanjing Tech University (NanjingTech), Nanjing, Jiangsu, China. ²Institute of Polymer Optoelectronic Materials and Devices, State Key Laboratory of Luminescent Materials and Devices, South China University of Technology, Guangzhou, P. R. China. ³Frontiers Science Center for Flexible Electronics, Institute of Flexible Electronics (IFE), Northwestern Polytechnical University, Xi'an, China. ✉e-mail: iamydxia@njtech.edu.cn; iamqxguo@njtech.edu.cn; iamyhchen@njtech.edu.cn; provost@nwpu.edu.cn

using thin phenylethanamine bromide layers[17]. Despite these advancements, the performance of thermally evaporated red PeLEDs continues to lag behind. This limitation hinders the commercialization of PeLEDs for display applications. Therefore, advancing the development of red PeLEDs through thermal evaporation has become a critical priority.

Currently, most reported thermally evaporated PeLEDs are fabricated using a multi-source co-evaporation technique, which faces several challenges. First, co-evaporation is inherently an in-situ crystallization process, making it difficult to control. Second, the complexity of the process increases due to the diverse components of perovskite precursors and additives, typically exceeding three (co-evaporating CsBr, PbBr$_2$, and TPPO for green PeLED)[13]. Additionally, stabilizing the evaporation rate of ammonium salts (e.g., MABr, FABr) is challenging, further complicating the process[18–20]. In contrast, the technique of layer-by-layer (LBL) evaporation followed by post-annealing for reaction and crystallization is simpler, more efficient, and exhibits better reproducibility, making it more suitable for large-area and scale production[21]. Given that perovskite emissive thin films are typically only tens of nanometers thick, complete and uniform diffusion and reactions can be easily achieved through annealing. Thus, for LBL evaporation, a deep understanding of diffusion, reaction, and crystallization dynamics, as well as precise control over the crystallization process, is critical for producing high-quality perovskite emission films. Despite the significant potential of LBL evaporation, research in this area remains very limited[20,21]. The current quality of the films and the performance of the devices are relatively low due to a lack of profound understanding of the crystallization mechanisms, which urgently need to be improved.

In this work, we employ an LBL evaporation technique to sequentially deposit the organic halide formamidine hydroiodide (FAI), the metal halide CsBr, 5-aminovaleric acid (5-AVA) additive, and the metal halide lead iodide (PbI$_2$) as the solid precursor. Through a subsequent post-annealing process, we achieve the complete diffusion, reaction, and crystallization of the thin solid precursor layer (~50 nm) to form high-quality perovskite thin films. We note that the introduction of 5-AVA could effectively suppress in-situ interfacial reactions during vacuum deposition and slow down the crystallization process during post-annealing, significantly enhancing the crystalline quality of perovskite thin films. Additionally, 5-AVA could form coordination bonds with uncoordinated Pb^{2+}, suppressing defect-induced non-radiative recombination. The optimized emission film exhibits uniform optoelectronic properties with improved radiative recombination efficiency. As a result, we achieve the efficient fully thermal evaporated red-PeLEDs (Cs$_x$FA$_{1-x}$PbIyBr$_{3-y}$), with a maximum EQE of 9% and a brightness exceeding 1500 cd m^{-2} (670 nm). LBL evaporation allows for continuous tuning of emission spectra by controlling the elemental ratios. The resulting deep-red PeLED (Cs$_x$FA$_{1-x}$PbI$_3$) shows an EQE of 7.27% (730 nm) and a high radiance of 204.71 W s^{-1} m^{-2}. Moreover, by taking advantage of the large-area uniformity of the sequential thermal evaporation, we realize large-area (50 × 50 mm^2) and patterned emissive thin films and devices. This provides a scalable and cost-effective approach for the production of high-performance PeLEDs, bridging the gap toward their commercialization in next-generation display and lighting technologies.

Results and discussion
Crystallization process of evaporated perovskite
Figure 1a illustrates the fabrication process of FA$_x$Cs$_{1-x}$PbI$_y$Br$_{3-y}$ perovskite thin films through LBL evaporation. In this process, the sequential deposition method involves evaporating solid precursor materials of FAI, CsBr, 5-AVA, and PbI$_2$ layer-by-layer. A quartz crucible with a beam-source heating configuration was employed to ensure stable evaporation of FAI and 5-AVA (Supplementary Fig. 1). No obvious decomposition was observed during the evaporation process

(Supplementary Fig. 2). The stoichiometric ratio of the solid precursor was realized by precisely controlling the thickness of each layer, ensuring good process reproducibility and large-area uniformity. The annealing temperature was optimized according to the photoluminescence (PL) properties (Supplementary Fig. 3). We note that the perovskite annealing temperature did not cause damage to the underlying self-assembled monolayers (SAMs) layer (Supplementary Fig. 4)[22,23]. Here, 5-AVA with optimized thickness (Supplementary Fig. 5) was introduced to manipulate the reaction and crystallization process. As shown in Fig. 1b and Supplementary Fig. 6, the perovskite thin film w/o 5AVA (control) showed a faint red light under UV illumination and weak perovskite X-ray diffraction (XRD) peaks before the annealing process. Due to the higher energy carried by vaporized molecules, in-situ reactions at the interface between CsBr and PbI$_2$ layers occurred before annealing, which cannot be resolved by simply reducing the evaporation rate (Supplementary Fig. 7). The formation of perovskite at the interface reactions hindered the sufficient diffusion and reaction of the solid precursor during the subsequent annealing process. This led to poor crystalline quality of the perovskite thin films (Supplementary Fig. 6) and low PL intensity (Fig. 1b). In contrast, no emission was observed in the perovskite thin film w/ 5AVA (target) under UV illumination, demonstrating that the addition of 5-AVA effectively inhibited the in-situ reactions between the solid precursor. After the subsequent annealing process, the PL intensity of the target film was significantly improved compared to the control (Fig. 1b). This was attributed to the complete diffusion, reaction, and crystallization process through the control over the annealing process. As demonstrated by the Grazing-incidence wide-angle X-ray scattering (GIWAXS) measurements (Fig. 1c, d), a continuous Debye–Scherrer diffraction ring was observed at $q = 10$ nm^{-1} in both control and target films, corresponding to the (100) diffraction peak[24]. Notably, the target film showed sharper and stronger Bragg spots than the control, indicating that the addition of 5-AVA could enhance the crystallinity, which was further demonstrated by the XRD measurements (Supplementary Fig. 6). In addition, a weak diffraction ring of the residual intermediate around $q = 7.5$ nm^{-1} could be observed in the control film, because of the insufficient diffusion and reaction. We further performed scanning electron microscope (SEM) analysis in Fig. 1e, f. The target film exhibited better crystallinity and a more uniformly distributed grain size. The cross-section (Supplementary Fig. 8) and bottom (Supplementary Fig. 9) SEM images further demonstrated the dense perovskite crystal film. The energy dispersive X-ray spectroscopy (EDS) mapping demonstrated the uniform distribution of Cs, Pb, Br, and I elements, confirming the complete reaction in the solid precursor deposited by LBL evaporation (Supplementary Fig. 10).

To investigate the mechanism of crystallization kinetics during the annealing process, in situ ultraviolet-visible absorption spectroscopy tests were conducted. Both target and control perovskite films showed two characteristic stages, as shown in Fig. 1g, h. The first stage, characterized by increased intensity, corresponded to the reaction and initial perovskite crystal growth process. The control film exhibited a very fast crystallization rate, completing in just 17 s. In contrast, after introducing a 5-AVA layer, the perovskite crystallization time was extended to over 50 s, which contributed to better control and orderliness of the crystallization process. The different crystallization rates were also confirmed by in-situ PL measurements (Supplementary Fig. 11), where the target film took longer to reach its maximum PL intensity. In the second stage, the absorption and PL intensity of the target film increased more slowly with prolonged annealing, indicating a crystallization enhancement process. We extracted the time-resolved absorption intensity in Supplementary Fig. 12. For the control film, the absorption intensity would gradually decrease, which might be caused by the formation of defects. Therefore, 5-AVA could retard the crystallization rate and enhance the crystallization quality of the evaporated perovskite films. LBL evaporation could easily realize the tuning
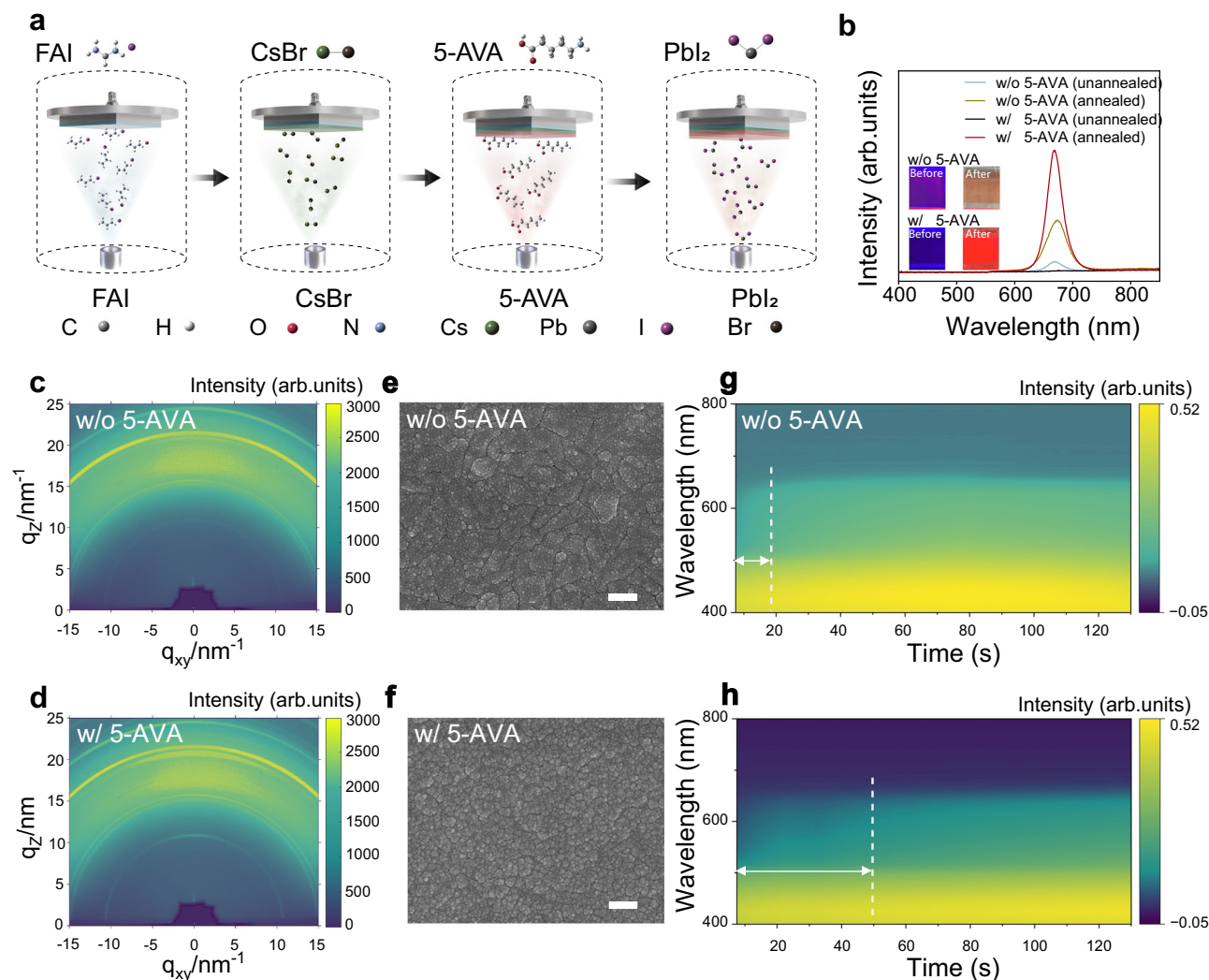
Fig. 1 | Layer-by-layer evaporation crystallization process of perovskite thin films. a Schematic diagram of sequential thermal evaporation of perovskite thin films. **b** The PL intensity of perovskite thin films w/o 5-AVA and w/ 5-AVA before and after annealing. The inserts are the photographs of the perovskite films before and after thermal annealing. **c**, **d** GIWAXS patterns of perovskite thin films (**c**) w/o 5-AVA and (**d**) w/ 5-AVA. **e**, **f** SEM images of (**e**) w/o 5-AVA and (**f**) w/ 5-AVA perovskite thin films. The scale bar represents 200 nm. **g**, **h** In-situ UV–vis absorption spectra of perovskite thin films (**g**) w/o 5-AVA and (**h**) w/ 5-AVA during the annealing process.

of PL spectra by controlling the elemental ratios. For example, we replaced the CsBr layer with CsBr/CsI in varying thickness ratios[25], achieving continuous tuning of the PL spectra from 670 nm to 730 nm (Supplementary Fig. 13).

Defect passivation effect of 5-AVA in perovskite films

5-AVA possessed Lewis-base property, which enabled it to form a strong coordination interaction with PbI_2. This could not only slow down the crystallization process and improve the quality of crystallization, but also effectively passivate perovskite defects, thereby enhancing the luminescence efficiency. The Fourier transform infrared (FTIR) spectroscopy was employed to elucidate the interaction between 5-AVA and the perovskite precursor. As shown in Fig. 2a, the pure 5-AVA powder exhibited the characteristic C=O stretching vibration peak at 1638 cm^{-1}. Notably, when 5-AVA is mixed with PbI_2, the C=O stretching vibration peak shifted to a lower wavenumber at 1635 cm^{-1}, indicating a strong bonding interaction between Pb^{2+} and $-COO^-$ [26,27]. The interaction between 5-AVA and perovskite was further verified by X-ray photoelectron spectroscopy (XPS). As shown in Fig. 2b, c, the Pb-*4f* spectrum exhibited two distinct peaks located at 138.8 eV (Pb-4$f_{7/2}$) and 143.6 eV (Pb-4$f_{5/2}$). After introducing 5-AVA, the binding energy was reduced by approximately 0.2 eV, with these two peaks shifting to 138.6 eV and 143.4 eV, respectively. We

also observed that the binding energies of the I-3$d_{5/2}$ and I-3$d_{3/2}$ orbitals decreased from 619.4 eV and 630.9 eV to 619.1 eV and 630.6 eV, respectively, with an overall reduction of approximately 0.3 eV. The interaction between 5-AVA and PbI_2 was also confirmed by the ^{13}C nuclear magnetic resonance spectroscopy (NMR) measurements Fig. 2d). These results indicated that the C=O group in 5-AVA donated the lone-pair electrons of oxygen to the empty 6p orbital of Pb^{2+}, thereby altering the electrostatic interaction between Pb^{2+} and I^- ions[28,29]. In addition to coordinating with Pb^{2+}, 5-AVA also exhibited interaction with FAI. Supplementary Fig. 14 shows the FTIR spectra of pure 5-AVA powder, pure FAI powder, and the mixture of 5-AVA and FAI. The N–H stretching vibration ($v_{(N-H)}$) of FAI shifts from 3367 cm^{-1} to a lower wavenumber at 3352 cm^{-1}. This indicated that 5-AVA can also form hydrogen bonds with FAI, contributing to slowing down the crystallization.

The defect state density (n_t) in perovskite thin films could be determined through space-charge-limited current (SCLC) measurements[30]. By obtaining the trap-filled limit voltage (V_{TFL}), the n_t could be calculated through the following equation:

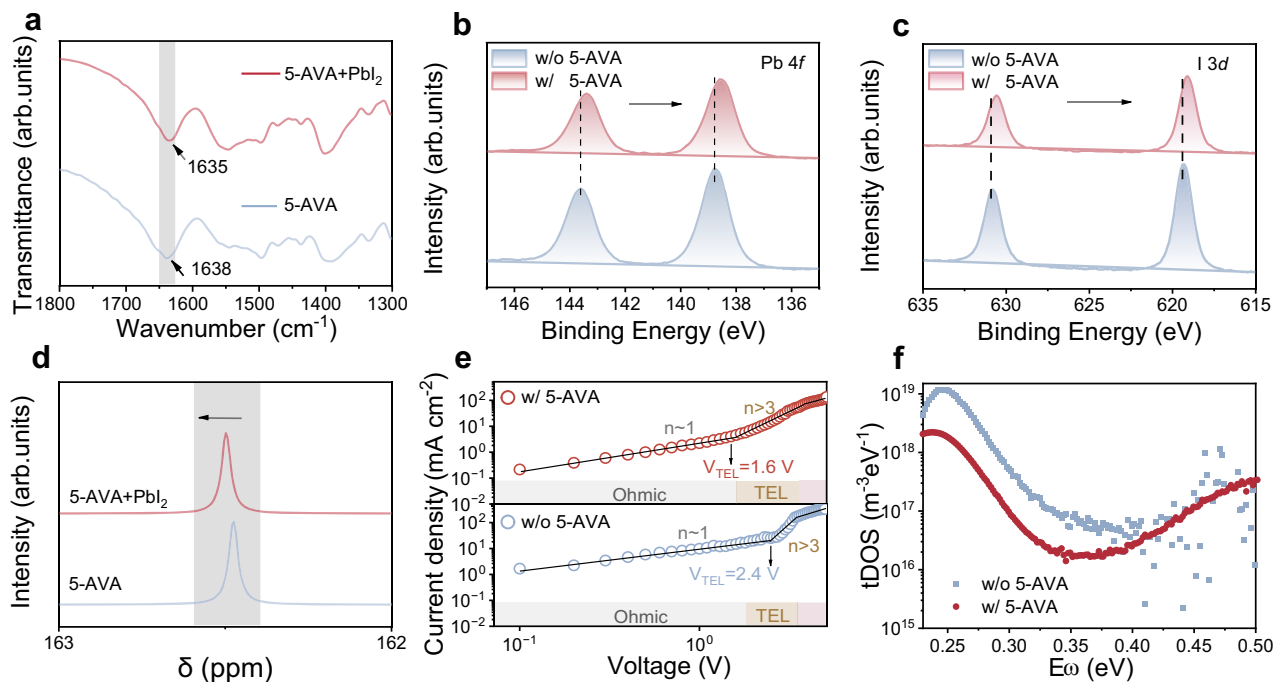$$n_t = \frac{2\varepsilon_r \varepsilon_0 V_{TFL}}{q^{D^2}} \quad (1)$$

Fig. 2 | The interaction mechanism between 5-AVA and perovskite. a FTIR spectra of pure 5-AVA and 5-AVA+PbI$_2$ mixture, where the characteristic C=O stretching vibration peak is marked by gray squares. **b**, **c** XPS spectra of (**b**) Pb 4f and (**c**) I 3d for perovskite thin films w/ 5-AVA and w/o 5-AVA. **d** ^{13}C NMR spectra of pure 5-AVA and 5-AVA+PbI$_2$ mixture. The gray squares highlight the characteristic peaks of 5-AVA. **e** SCLC measurements of the only-hole devices. **f** The trap density of states (tDOS) spectra of perovskite thin films.

Where q, D, ε_r, and ε_0 are the elementary charge, the thickness of the perovskite layer, the dielectric constant of the perovskite layer, and the vacuum permittivity, respectively. As shown in Fig. 2e, after the introduction of 5-AVA, the V_{TFL} of the perovskite layer decreased from 2.4 V to 1.6 V. The experimental data clearly indicate that the trap density of states (n_t) of the target film was significantly reduced to 3.3×10^{18} cm^{-3}, compared to 4.97×10^{18} cm^{-3} for the control. This was further confirmed by the trap density of states (tDOS) measurements in Fig. 2f, where the target perovskite thin film exhibited a much lower trap density than the control over the entire energy range. These findings underscore the importance of 5-AVA as a multifunctional agent in manipulating the crystallization process and passivating defects[31].

Photophysical properties of the perovskite thin films

We then sought to investigate the optoelectronic properties of the sequentially LBL evaporated perovskite thin films. We studied the PL uniformity of the films by conducting confocal PL intensity mapping measurements. As shown in Fig. 3a, b, the films exhibited good PL uniformity overall, indicating the advantage of LBL evaporation. After the introduction of 5-AVA, the PL intensity and distribution uniformity were further enhanced, as shown in the inset is a plot of the statistical PL intensity distribution. We note that the peak positions and the corresponding absorption spectrum remained unchanged after the incorporation of 5-AVA (Supplementary Fig. 15), indicating that 5-AVA did not alter the PL characteristics. We also employed laser scanning confocal microscopy to evaluate the PL lifetime mapping of the films (Fig. 3c, d). The target film demonstrated a longer average lifetime. These results indicated that 5-AVA could improve the film crystallinity and decrease the trap density. To demonstrate the vertical uniformity of the thin film, we conducted steady-state fluorescence spectra and PL lifetime measurements on both sides of the films. As shown (Fig. 3e, f), the PL intensity emitted from both sides of the target film was identical and higher than the

control film. Similar results could be obtained from the TRPL measurements (Supplementary Table 1). We thus concluded that LBL evaporation can produce perovskite luminescent thin films with good uniformity in both lateral and vertical directions. By combining 5-AVA-based crystallization regulation and post-annealing process control, it is possible to achieve the full reaction and crystallization of solid-phase precursors deposited by LBL evaporation, resulting in high-quality perovskite crystal thin films.

We conducted transient absorption (TA) measurements to explore the carrier dynamics. Under 375 nm excitation, the target perovskite thin film exhibited a single ground-state bleaching (GSB) signal at approximately 670 nm (Fig. 3g, Supplementary Fig. 16, Supplementary Fig. 17, and Supplementary Fig. 18), consistent with its steady-state absorption peak. For 3D perovskite thin films where the primary carrier type is free carriers, the carrier dynamics can be described by the following equation:

$$-\frac{dn(t)}{dt} = k_3 n^3 + k_2 n^2 + k_1 n \tag{2}$$

where n represents the charge carrier density; k_1 is the trap-mediated non-radiative recombination rate constant; k_2 is the bi-molecular recombination rate constant; and k_3 is the Auger recombination rate constant[32–35]. Under low pump fluence, k_1 could typically be extracted from the tail of TRPL data. k_2 and k_3 could be extracted from the well-established global fitting of the transient absorption dynamics (Fig. 3h). Global fitting was performed on the power-dependent TA data, and fitting results were summarized in Supplementary Table 1. As shown, the introduction of 5-AVA not only reduced the trap-mediated non-radiative recombination rate constant ($k_{1target} = 7.76 \times 10^7$ s^{-1}, $k_{1control} = 1.14 \times 10^8$ s^{-1}) but also significantly enhanced the bi-molecular recombination rate constant ($k_{2target} = 9.67 \times 10^{11}$ s^{-1}, $k_{2control} = 7.02 \times 10^{11}$ s^{-1}). Meanwhile, k_3 is lower compared to the control film, suggesting a reduced Auger recombination constant.
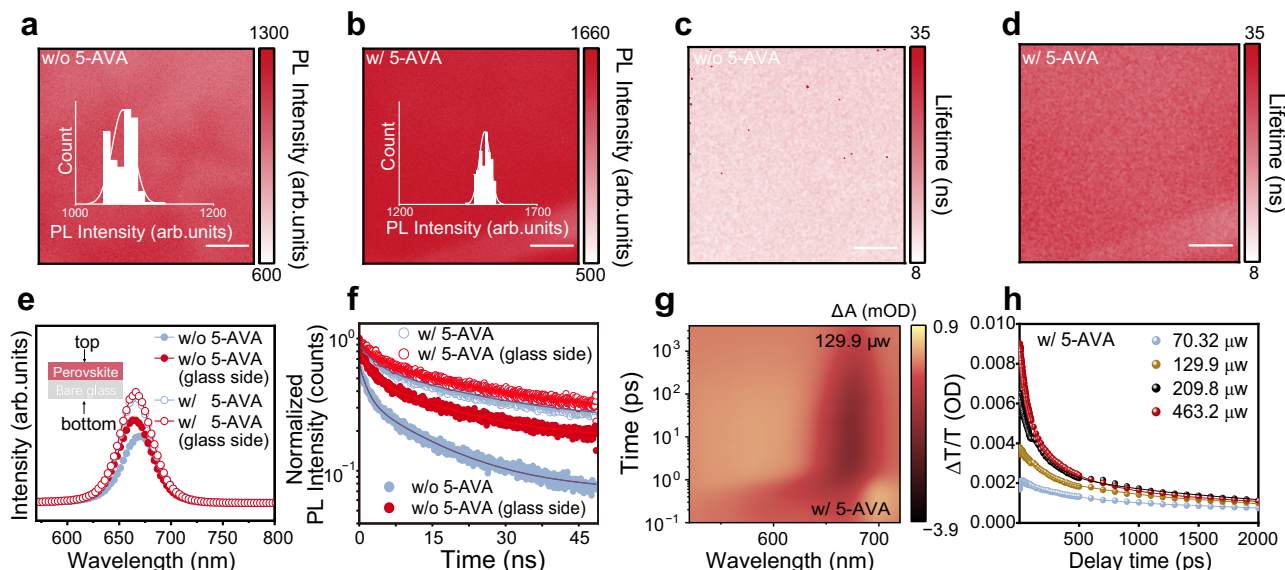
Fig. 3 | Optoelectronic characterization of perovskite thin films. a, b PL mapping of the perovskite thin films (**a**) w/o 5-AVA and (**b**) w/w/ 5-AVA, with insets showing the PL intensity distribution statistics for each film. The scale bar represents 10 μm. **c, d** TRPL mapping of the perovskite thin films (**c**) w/o 5-AVA and (**d**) w/ 5-AVA films. The scale bar represents 10 μm. **e, f** Steady-state PL spectra (**e**) and TRPL spectra (**f**) of perovskite thin films deposited on bare glass w/o 5-AVA and w/5-AVA (excitation from both the perovskite and glass sides). **g** TA measurements of perovskite thin film w/ 5-AVA under the excitation pump fluence of 129.9 μW. **h** TA intensity decay curves and the global fitting results of perovskite thin film w/ 5AVA at different powers.

Device performance of perovskite light-emitting diodes

We then employed the LBL-evaporated perovskite thin film to fabricate the PeLEDs with a device structure of ITO/2PACz/perovskite (50 nm)/TPBi (40 nm)/LiF/Al (100 nm) (Fig. 4a). The current density–voltage–luminance (J–V–L) curves of the PeLED devices were shown in Fig. 4b. The turn-on voltage decreased from 3.00 V of the control device (w/o 5-AVA) to 2.75 V of the target device (w/ 5-AVA). The target and the control devices exhibited comparable current density. The turn-on voltage was a bit higher, which could potentially stem from excessively large injection barriers resulting from trace precursor residue and the need for further improvement in film crystallinity. However, the target device exhibited a much higher maximum luminance (L_{max}) of 1524 cd m^{-2}, compared to the control device (L_{max} = 1081 cd m^{-2}). More importantly, the target device yielded an obviously enhanced maximum EQE of 9.00% (Fig. 4c), which represented the highest level among the reported thermal-evaporated red-PeLEDs (Fig. 4d and Supplementary Table 2).

We monitored the electroluminescence (EL) spectrum of the target PeLED with the applied voltage range from 2.5 V to 4.5 V. The emission peak remained consistently at 670 nm, indicating the negligible ion migration or phase segregation (Fig. 4e). We also replaced CsBr with CsI to fabricate deep-red Cs$_x$FA$_{1-x}$PbI$_3$-PeLEDs, resulting in a shift of the spectra wavelength from 670 nm to 730 nm. The Cs$_x$FA$_{1-x}$PbI$_3$-PeLED showed an EQE and radiance of 7.27% and 204.71 W s^{-1} m^{-2}, respectively. This demonstrated the versatility of LBL evaporation as an efficient and straightforward technique for fabricating high-performance PeLEDs (Fig. 4f and Supplementary Fig. 19). The effect of 5-AVA thickness on red-PeLEDs was shown in Supplementary Fig. 20. The inset of Fig. 4c showed a working image of a FA$_x$Cs$_{1-x}$PbI$_y$Br$_{3-y}$-PeLED under forward bias. It emitted a vivid deep-red light with a peak of 670 nm and FWHM of 33 nm, which matched well with its PL spectra. The target device showed a CIE color coordinate of (0.714, 0.281), approaching the recommended Rec. 2020 standard for red emitters (Fig. 4g). We further assessed the long-term operational color-stability of the device by monitoring the changes in its emission spectrum and CIE coordinates under different applied voltages and continuous working conditions. As illustrated in Supplementary Fig. 21 and Supplementary Fig. 22, the device

demonstrated good stability in both its emission spectrum and CIE coordinates. The stable deep-red emission held great potential for future wide color-gamut display. The target device exhibited a longer operational lifetime of 255 min under a constant current density of 30 mA cm^{-2}, compared to 81 min for the control (Supplementary Fig. 23). The enhancement in luminance and EQE should be attributed to the improved film quality through employing 5-AVA. We collected efficiency data from 20 devices and obtained an average EQE of 7.13%, as shown in the histogram in Fig. 4h, confirming good reproducibility.

To further validate the uniformity and scalability of the sequential LBL evaporation technique, we successfully fabricated a large-area (2500 mm^2) FA$_x$Cs$_{1-x}$PbI$_y$Br$_{3-y}$ perovskite thin film, as shown in Fig. 5a. The as-prepared film exhibited uniform PL emission across the entire macroscopic area under UV illumination. To quantitatively evaluate the uniformity, we selected 16 evenly distributed positions across the thin film (indicated in the inset of Fig. 5a) and measured the PL intensities and shapes at these locations (Fig. 5b). The analysis revealed highly consistent PL intensities across all measured positions, with only minimal fluctuations in the PL peak positions (Fig. 5c). This result underscored the advantages of the LBL evaporation technique in producing high-quality and large-scale uniform perovskite thin films and devices.

We thus fabricated the large-scale PeLED with an active area of 150 mm^2 (15 mm × 10 mm). As shown in Fig. 5d, it exhibited bright deep-red emission with high uniformity under forward applied voltages. By combining the mask process, we also realized the patterned EL devices with customized patterns of "IAM" and landmark building (*Nanjing Tech TianBao Pavilion*) of Nanjing Tech University in the sizes of 150 mm^2 (15 mm × 10 mm) and 2500 mm^2 (50 mm × 50 mm), respectively. Figure 5e, f displayed the vivid photographs of the devices in operation, showing homogeneous light emission and excellent preservation of the designed mask pattern. This work is expected to promote the application of PeLEDs in display and lighting.

Discussion

In summary, we successfully demonstrated a facile LBL evaporation technique for fabricating efficient and large-area PeLEDs. The introduction of 5-AVA as an additive has proven to be a critical factor in regulating the crystallization dynamics of the evaporated perovskite
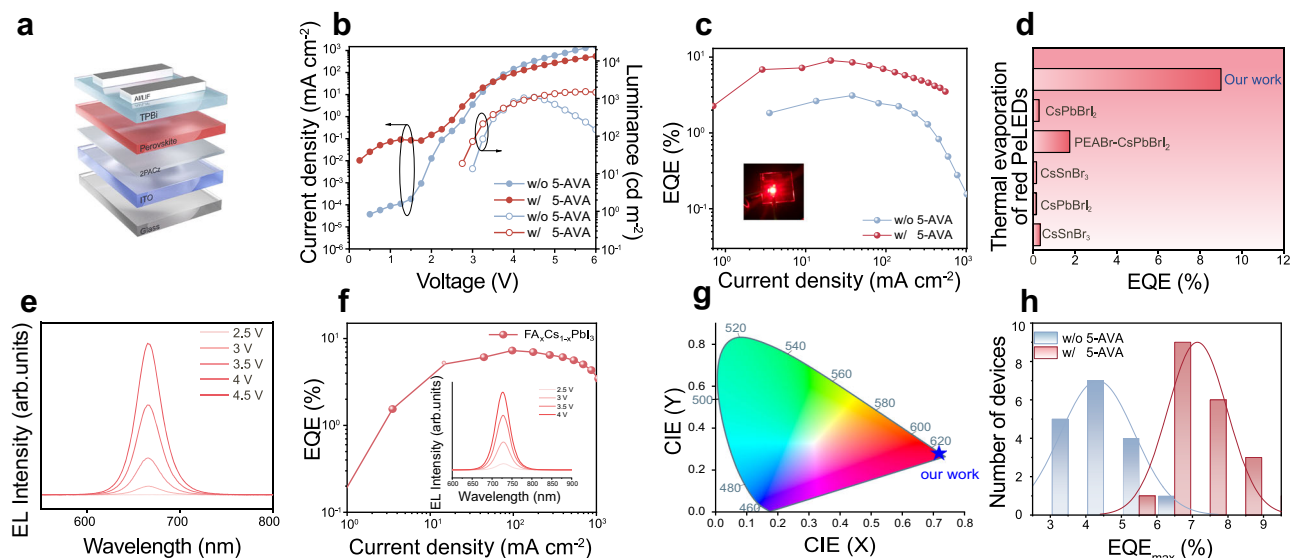
Fig. 4 | Device structure and performance of PeLEDs. a Device structure of the red PeLEDs. **b** Current density–voltage and luminance–voltage characteristics of PeLEDs w/o 5-AVA and w/ 5-AVA. **c** EQE-Current density curves of PeLEDs w/o 5-AVA and w/ 5-AVA, with inset showing the photo of PeLED during operation. **d** Summary EQE performance of previously reported thermally evaporated red PeLEDs. **e** EL spectra of PeLEDs w/ 5-AVA under an applied voltage ranging from 2.5 V to 4.5 V. **f** EQE-Current density curves of $Cs_xFA_{1-x}PbI_3$-PeLEDs, with the inset showing the EL spectra of PeLEDs under an applied voltage ranging from 2.5 V to 4 V. **g** CIE diagram of target red PeLEDs. **h** Histogram of peak EQEs for PeLEDs w/o 5-AVA and w/ 5-AVA.

films and improving their optoelectronic performance. It could effectively suppress in-situ interfacial reactions and slow down the crystallization process, leading to improved crystallinity. Besides, C=O group in 5-AVA could coordinate with Pb^{2+} to reduce the trap density. Utilizing this strategy, we realized the efficient and uniform deep-red $FA_xCs_{1-x}PbI_yBr_{3-y}$ perovskite thin film with tunable emission spectra. The resulting PeLEDs achieved an EQE of 9% and a maximum luminance of 1524 cd m^{-2}, representing the state-of-the-art thermal-evaporated red-PeLEDs reported to date. We also realized the $FA_xCs_{1-x}PbI_3$-PeLED with an EQE of 7.27% to demonstrate the versatility of the LBL technique. Furthermore, the LBL evaporation enabled the fabrication of large-area (50 × 50 mm^2) and patterned perovskite thin films and devices for high-quality display and lighting applications. This work will inspire further research and development efforts toward enhancing the performance of thermally evaporated PeLEDs and promoting their final commercialization.

Methods
Materials
The precursor materials used for the thermal evaporation of perovskite thin films, including formamidine iodide (FAI, 99.9%), cesium bromide (CsBr, 99.999%), lead iodide (PbI$_2$, 98%), and 5-aminovaleric acid (5-AVA, 97%), were purchased from GreatCell Solar Materials, TCI, Advanced Election Technology, and Aladdin, respectively. Other materials used in this work, including [2-(9H-carbazol-9-yl) ethyl] phosphonic acid (2PACz, 98%), 1,3,5-Tri[(3-pyridyl)-phen-3-yl] benzene (TPBi, 99.5%), lithium fluoride (LiF, 99.9%), and metallic aluminum (99.99%), were obtained from TCI, Jilin OLED Photoelectric Material, Sigma-Aldrich, and Zhong-Nuo Advanced Material Technology, respectively.

Perovskite thin film preparation
The pretreated substrates were transferred into a vacuum evaporation chamber for the thermal evaporation of perovskite thin films. The evaporation temperature of each source was precisely controlled by adjusting the current applied to the heating source, allowing for accurate regulation of precursor deposition rates. The evaporation rates of all components were monitored in real time using a quartz crystal micro-balance. Once the deposition rate stabilized at the target value, the

substrate shutter was opened to begin the deposition. The optimized thicknesses and deposition rates for the individual precursor layers were FAI (90 Å, 0.5 Å s^{-1}), CsBr (250 Å, 1 Å s^{-1}), 5-AVA (15 Å, 0.1 Å s^{-1}), and PbI$_2$ (280 Å, 1 Å s^{-1}). For the $FA_xCs_{1-x}PbI_3$ perovskite system, the deposition rates of FAI, CsI, and PbI$_2$ were maintained at 0.5 Å s^{-1}, 1 Å s^{-1}, and 1 Å s^{-1}, respectively. During the entire deposition process, the vacuum level in the chamber was maintained below 5×10^{-4} Pa. The substrate holder was rotated at a constant speed to ensure uniform film deposition. After the evaporation of all precursors was completed, the samples were transferred to a nitrogen-filled glovebox and annealed at 90 °C for 10 min. For large-area film fabrication, un-patterned ITO glass substrates with a size of 50 mm × 50 mm (Advanced Election Technology Co., Ltd., China) was used. The cleaning and pretreatment procedures were identical to those used for small-area substrates. 2PACz was evaporated on the ITO substrates via thermal evaporation at a rate of 0.1 Å s^{-1} to a final thickness of 30 Å, followed by annealing at 100 °C for 10 min. The substrates were then transferred back to the perovskite deposition chamber, where FAI, CsBr, 5-AVA, and PbI$_2$ were sequentially evaporated following the same procedure. Finally, the annealing step at 90 °C for 10 min was carried out.

PeLED fabrication
ITO-coated glass substrates (Advanced Election Technology Co., Ltd., China) were sequentially cleaned by ultrasonication in detergent solution, deionized water, and anhydrous ethanol. The substrates were then dried using high-purity nitrogen and baked in an oven to completely remove any residual solvent. Afterward, the substrates were treated with oxygen plasma for 1 min before spin-coating. A solution of 2PACz in isopropanol (IPA) was spin-coated onto the substrates at 4000 rpm for 30 s, followed by thermal annealing at 100 °C for 10 min. Afterward, perovskite precursor layers were sequentially deposited onto the 2PACz-modified substrates via thermal evaporation, and the films were annealed at 90 °C for 10 min. After the perovskite deposition, the substrates were transferred to another vacuum chamber for thermal evaporation of the TPBi (40 nm), LiF (1 nm), and Al (100 nm) under high vacuum (<5×10^{-4} Pa). For large-area patterned devices, the same TPBi (40 nm)/LiF (1 nm)/Al (100 nm) layers were deposited on the large-area perovskite films, and the Al electrodes were patterned using a pre-designed shadow mask to define the device structure and
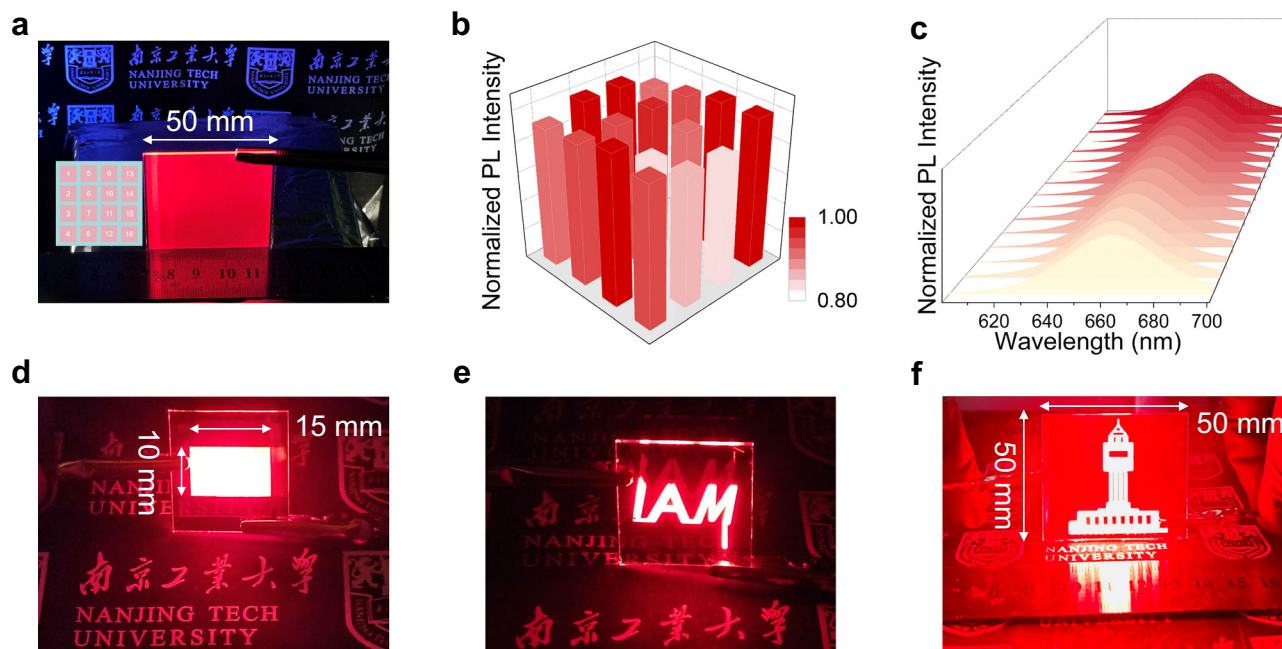
Fig. 5 | Large-area and patterned PeLEDs. a PL image of a 50 × 50 mm² perovskite thin film fabricated via LBL deposition, with the inset showing 16 selected points for uniformity evaluation. **b** PL intensity distribution at 16 positions. **c** PL peak positions at 16 locations. **d** EL image of a PeLED with an emission area of 15 × 10 mm². **e** PeLEDs with "IAM" patterned design. **f** PeLEDs with a patterned design resembling the landmark building of Nanjing Tech University.

obtain the desired PeLED patterns. For hole-only devices, the architecture was ITO/2PACz/perovskite/NPB (50 nm)/MoO₃ (20 nm)/Al. NPB and MoO₃ were evaporated at rates of $1\,\text{Å}\,\text{s}^{-1}$ and $0.1\,\text{Å}\,\text{s}^{-1}$, respectively. The preparation procedures for the substrates and perovskite films were the same as described above.

Film and device characterization
Steady-state photoluminescence (PL) spectra were measured using a Hitachi F-4600 fluorescence spectrophotometer. Grazing-incidence wide-angle X-ray scattering (GIWAXS) characterization was performed by beamline 14B of the Shanghai Synchrotron Radiation Facility (SSRF), with an incident X-ray beam of $\lambda = 1.2398\,\text{Å}$. Scattering signals were collected using a MarCCD detector positioned 268.886 mm vertically from the sample. X-ray diffraction (XRD) patterns were carried out using a Bruker AXS D8 equipped with a Cu Kα X-ray source. The surface morphology of the perovskite films was tested by a field-emission scanning electron microscope (SEM, Hitachi Regulus8100). Ultraviolet-visible (UV-vis) absorption spectra were characterized with a Shimadzu UV-1780 spectrophotometer. Attenuated total reflectance Fourier-transform infrared (ATR-FTIR) spectra were collected on a Thermo Fisher IS50 spectrometer equipped with a reflection accessory. The JOEL nuclear magnetic resonance (NMR) spectrometer (JNM-ECZ400S, 400 MHz, Japan) was employed for NMR measurements. Time-resolved PL spectra were performed using an Edinburgh FS5-TCSPC system. PL mapping and PL lifetime mapping were carried out on a FILM 300 system (TIME TECH SPECTRA) using a 405 nm excitation source. Femtosecond broadband transient absorption (TA) spectra were measured using a HARPIA TA spectrometer (Ultrafast Systems). Electroluminescence (EL) measurements and stability tests of PeLEDs were performed using a measurement system composed of a Keithley 2400 source meter, QE65 Pro spectrometer, and a fiber optic integrating sphere (FOIS-1-TEF fiber), which was operated within a nitrogen-filled glovebox.

Data availability
All data needed to evaluate the conclusions in the paper are present in the main text and the Supplementary Information, or from the corresponding authors upon request. Source data are deposited in Figshare: https://doi.org/10.6084/m9.figshare.29067776.

References
1. Stranks, S. D. et al. Electron-hole diffusion lengths exceeding 1 micrometer in an organometal trihalide perovskite absorber. *Science* **342**, 341–344 (2013).
2. Gerber, E. E. et al. Integrin-modulating therapy prevents fibrosis and autoimmunity in mouse models of scleroderma. *Nature* **503**, 126–130 (2013).
3. Quan, L. N., de Arquer, F. P. G., Sabatini, R. P. & Sargent, E. H. Perovskites for light emission. *Adv. Mater.* **30**, 1801996 (2018).
4. Rahimnejad, S., Kovalenko, A., Fores, S. M., Aranda, C. & Guerrero, A. Coordination chemistry dictates the structural defects in lead halide perovskites. *Chemphyschem* **17**, 2795–2798 (2016).
5. Kim, Y.-H. et al. Comprehensive defect suppression in perovskite nanocrystals for high-efficiency light-emitting diodes. *Nat. Photonics* **15**, 148–155 (2021).
6. Zhu, L. et al. Unveiling the additive-assisted oriented growth of perovskite crystallite for high performance light-emitting diodes. *Nat. Commun.* **12**, 5081 (2021).
7. Tan, Z.-K. et al. Bright light-emitting diodes based on organometal halide perovskite. *Nat. Nanotechnol.* **9**, 687–692 (2014).
8. Li, M. et al. Acceleration of radiative recombination for efficient perovskite LEDs. *Nature* **630**, 631–635 (2024).
9. Baek, S.-D. et al. Grain engineering for efficient near-infrared perovskite light-emitting diodes. *Nat. Commun.* **15**, 10760 (2024).
10. Feng, S.-C. et al. Efficient and stable red perovskite light-emitting diodes via thermodynamic crystallization control. *Adv. Mater.* **36**, 2410255 (2024).
11. Sun, S.-Q. et al. Enhancing light outcoupling efficiency via anisotropic low refractive index electron transporting materials for efficient perovskite light-emitting diodes. *Adv. Mater.* **36**, 2400421 (2024).
12. Han, T.-H. et al. A roadmap for the commercialization of perovskite light emitters. *Nat. Rev. Mater.* **7**, 757–777 (2022).

13. Li, J. et al. Efficient all-thermally evaporated perovskite light-emitting diodes for active-matrix displays. *Nat. Photonics* **17**, 435–441 (2023).

14. Chen, B. et al. Dual-function self-assembled molecules as hole-transport layers for thermally evaporated high-efficiency blue perovskite light-emitting diodes. *Adv. Mater.* **37**, 2411451 (2024).

15. Yuan, F. et al. All-inorganic hetero-structured cesium tin halide perovskite light-emitting diodes with current density over 900 A cm^{-2} and its amplified spontaneous emission behaviors. *Phys. Status Solidi* **12**, 1800090 (2018).

16. Guo, S., Liu, H.-F. & Liu, Y.-F. Efficient all-inorganic red perovskite light-emitting diodes with dual-interface-modified perovskites by vapor deposition. *Opt. Lett.* **47**, 2694–2697 (2022).

17. Liu, N. et al. Fluorine-modified passivator for efficient vacuum-deposited pure-red perovskite light-emitting diodes. *Light Sci. Appl.* **14**, 118 (2025).

18. Kosasih, F. U. et al. Thermal evaporation and hybrid deposition of perovskite solar cells and mini-modules. *Joule* **6**, 2692–2734 (2022).

19. Turren-Cruz, S. H., Hagfeldt, A. & Saliba, M. Methylammonium-free, high-performance, and stable perovskite solar cells on a planar architecture. *Science* **362**, 449–453 (2018).

20. Chiang, Y.-H., Anaya, M. & Stranks, S. D. Multisource vacuum deposition of methylammonium-free perovskite solar cells. *ACS Energy Lett.* **5**, 2498–2504 (2020).

21. Li, H. et al. Sequential vacuum-evaporated perovskite solar cells with more than 24% efficiency. *Sci. Adv.* **8**, eabo7422 (2022).

22. Liu, M. et al. Compact hole-selective self-assembled monolayers enabled by disassembling micelles in solution for efficient perovskite solar cells. *Adv. Mater.* **35**, 2304415 (2023).

23. Bi, H. et al. Selective contact self-assembled molecules for high-performance perovskite solar cells. *eScience* **5**, 100329 (2025).

24. Niu, T. et al. Phase-pure α-FAPbI$_3$ perovskite solar cells via activating lead-iodine frameworks. *Adv. Mater.* **36**, 2309171 (2024).

25. Wang, S. et al. Suppressed recombination for monolithic inorganic perovskite/silicon tandem solar cells with an approximate efficiency of 23. *eScience* **2**, 339–346 (2022).

26. Liu, C. et al. Highly efficient quasi-2D green perovskite light-emitting diodes with bifunctional amino acid. *Adv. Opt. Mater.* **10**, 2200276 (2022).

27. Hui, W. et al. Stabilizing black-phase formamidinium perovskite formation at room temperature and high humidity. *Science* **371**, 1359–1364 (2021).

28. Kong, L. et al. Smoothing the energy transfer pathway in quasi-2D perovskite films using methanesulfonate leads to highly efficient light-emitting devices. *Nat. Commun.* **12**, 1246 (2021).

29. Liang, Y. et al. Synergetic dual-additive strategy for regulating crystallization and defect passivation of perovskite nanograin toward efficient light-emitting diodes. *Adv. Opt. Mater.* **13**, 2402290 (2025).

30. Gao, H. et al. Homogeneous crystallization and buried interface passivation for perovskite tandem solar modules. *Science* **383**, 855–859 (2024).

31. Chen, M. et al. "Freezing" intermediate phases for efficient and stable FAPbI$_3$ perovskite solar cells. *Energy Environ. Sci.* **17**, 3375–3383 (2024).

32. Wehrenfennig, C. et al. Charge-carrier dynamics in vapour-deposited films of the organolead halide perovskite CH$_3$N$_3$PbI$_{3-x}$Cl$_x$. *Energy Environ. Sci. Sci.* **7**, 2269–2275 (2014).

33. Chen, Z. et al. Recombination dynamics study on nanostructured perovskite light-emitting devices. *Adv. Mater.* **30**, 1801370 (2018).

34. Zhang, D. et al. Highly efficient red perovskite light-emitting diodes with reduced efficiency roll-off enabled by manipulating crystallization of quasi-2D perovskites. *Adv. Funct. Mater.* **32**, 2205707 (2022).

35. Zhang, D. et al. Efficient deep-red perovskite light-emitting diodes based on a vertical 3D/2D perovskite heterojunction. *Adv. Funct. Mater.* **34**, 2403874 (2024).

Author contributions

Y. Chen, Q. G. and Y. Xia conceived the idea and designed the experiments. Y. Chen, Q. G. and W. H. supervised the work. Y. L. carried out most of the device fabrication and characterizations. N. M., Y. Xu, J. L., Y. Cui, Z. W.,and X. K. helped in fabricating perovskite films. T. P. and X. M. assisted in absorption and luminance spectra measurements. B. Y., J. C., and D. M. helped in the transient absorption measurements. L. C. and Z. H. helped in data analysis and discussion. Y. L. and Q. G. wrote the first draft of the paper. All the authors discussed the results and commented on the paper.

Competing interests

The authors declare no competing interests.

Additional information

Supplementary information The online version contains supplementary material available at https://doi.org/10.1038/s41467-025-62282-z.

Correspondence and requests for materials should be addressed to Yingdong Xia, Qingxun Guo, Yonghua Chen or Wei Huang.

Peer review information *Nature Communications* thanks Zhanhua Wei, Fanglong Yuan and Mingjian Yuan for their contribution to the peer review of this work. A peer review file is available.

Reprints and permissions information is available at http://www.nature.com/reprints

Publisher's note Springer Nature remains neutral with regard to jurisdictional claims in published maps and institutional affiliations.